Journal of Analytical and Applied Pyrolysis 194 (2026) 107536

Contents lists available at ScienceDirect

Journal of Analytical and Applied Pyrolysis

journal homepage: www.elsevier.com/locate/jaap

Advancing activated carbon production: Utilizing pine pruning biochar via induction heating with CO_2 and iron-based catalysts

Ahmet Erdem [a,b,d,*], Muthanna H. Al-Dahhan [b,c,d,e], Ahmed Jasim [b,c,d]

[a] Institute of Energy Technologies, Gebze Technical University, Gebze 41400, Türkiye
[b] Multiphase Flows and Reactors Engineering and Education Laboratory (mFReel), Department of Chemical and Biochemical Engineering, Missouri University of Science and Technology, Rolla, MO 65409, United States
[c] Linda and Bipin Doshi Department of Chemical and Biochemical Engineering, Missouri University of Science and Technology, Rolla, MO 65409, United States
[d] Department of Mining and Nuclear Engineering, Missouri University of Science and Technology, Rolla, MO 65409, United States
[e] ACER CoE, Mohammed VI Polytechnique University (UM6P), Ben Guerir, Morocco

ARTICLE INFO

Keywords:
Induction heating
Activated carbon
Biochar
Pine pruning biomass
CO_2 activation

ABSTRACT

This study introduces an induction heating approach for producing activated carbon from biochar obtained by thermal degradation of pine pruning waste from timber-related industries, using CO_2 and iron-based catalysts as activation agents. Activation experiments were performed using a 10 kW high-frequency induction system (28–40 kHz) under continuous CO_2 flow (15 mL min^{-1}), with electric current intensities of 200, 300, 400, and 500 A (corresponding to 700–1100°C) and durations of 30, 60, and 90 min, employing 45 g of iron-based catalysts (Fe–Ni–Ti–C, 85:6:3:6 wt%) per 3 g biochar (15:1 w/w). Mass loss increased from 13.7 % (200 A, 30 min) to 84 % (500 A, 90 min), inversely correlating with product yield, which ranged from 86.3 % to 16 %, respectively, highlighting the critical trade-off between porosity enhancement and material retention. Correspondingly, Brunauer–Emmett–Teller (BET) surface area was significantly enhanced, rising from 47.38 m^2 g^{-1} in the thermally processed biochar to 607.21 m^2 g^{-1} under milder activation conditions (200 A, 30 min), and further increasing to 865.07 m^2 g^{-1} at optimized conditions (500 A, 60 min) though with reduced yield (20.3 %). Fourier-transform infrared (FT-IR) spectroscopy confirmed the introduction of oxygen-containing functional groups, notably carbonyl and hydroxyl functionalities, while scanning electron microscopy (SEM) demonstrated substantial porosity development. X-ray diffraction (XRD) analysis further revealed crystallographic changes attributed to catalytic activity and carbon gasification reactions. These findings demonstrate that induction-assisted CO_2 activation with iron-based catalysts offers a rapid (30–90 min vs. conventional 2–4 h), energy-efficient, and scalable route for converting low-value pine pruning waste (biochar yield: 17 wt%) into high-performance activated carbon (BET up to 865 m^2 g^{-1}), suitable for water treatment, gas adsorption, and energy storage applications, while reducing reliance on chemical activators and minimizing environmental impact.

1. Introduction

Activated carbon is a highly versatile material with broad applications in water treatment, air purification, environmental remediation, industrial processing, and energy storage [1,2]. Its high surface area (often exceeding 600 m^2 g^{-1}) and well-developed porosity make it a critical resource for adsorption, catalysis, and filtration technologies [3–5]. However, conventional methods of producing activated carbon are resource-intensive, relying on significant energy consumption and non-renewable precursors, thereby presenting substantial environmental challenges [6–8]. These concerns drive the search for innovative and sustainable production techniques [9–12].

In recent years, biochar, derived from the thermal degradation of biomass, particularly through processes such as gasification and pyrolysis, has gained recognition as a sustainable precursor for activated carbon due to its renewability, carbon-neutral nature, economic feasibility, and waste valorization potential [13,14]. Among various forms of lignocellulosic residues, forestry byproducts such as pine pruning waste, a secondary product of timber management, represent an underutilized resource, with global forestry activities generating millions of tons annually [15–17]. These residues embody an abundant and untapped biomass source. Prior works spanning pistachio shells, cotton stalks,

* Corresponding author at: Institute of Energy Technologies, Gebze Technical University, Gebze 41400, Türkiye.
E-mail address: aerdem@gtu.edu.tr (A. Erdem).

https://doi.org/10.1016/j.jaap.2025.107536
Received 19 August 2025; Received in revised form 29 October 2025; Accepted 1 December 2025
Available online 2 December 2025

acorn shells, and other residues collectively corroborate the cost–performance motivation for low-cost precursors and optimized activation workflows [18,19].

Specifically, pine pruning waste, produced continuously in large quantities by global forestry and timber-related industries, underscores the urgent need for innovative approaches to convert such residues into value-added products [20]. Currently, in regions with abundant pine residues such as Lufkin, Texas substantial amounts of biomass waste accumulate, including pine sawdust, pruning residues, and by-products from the timber industry [21,22]. The effective valorization of these waste materials holds significant importance in terms of environmental sustainability and resource efficiency, presenting both a challenge and an opportunity for sustainable material development and circular economy strategies [23–25]. Transforming this waste into high-performance activated carbon not only mitigates disposal challenges but also aligns with the principles of a circular economy by yielding value-added products [26]. Additionally, biochar serves as a critical intermediate for producing activated carbon, which is increasingly in demand for applications such as environmental remediation, catalysis, and energy storage, while also playing a significant role in carbon sequestration [27,28].

Traditional activation techniques, including physical activation using pyrolysis with steam or CO_2 and chemical activation with agents like KOH or H_3PO_4, are constrained by lengthy process times and high energy demands [29,30]. Recently, alternative studies have reported the low-temperature activation of agricultural and forestry biomass wastes, such as corn cobs, rice husks, straw, and sawdust, using H_2SO_4 as the activating agent in chlorinated solvents [31]. However, these methods are constrained by prolonged processing times and substantial chemical consumption. Recent advances in carbonization and activation techniques demonstrate that microwave and induction assisted pyrolysis of lignocellulosic biomass are promising thermal methods due to their enhanced efficiency, sustainability, and process controllability [32–36]. Unlike conventional heating methods, induction heating uses electromagnetic fields to generate heat directly within or around the material, offering unparalleled precision in energy delivery. This feature makes it particularly suited for processes requiring localized or rapid heating, as it minimizes heat loss, directly transmits energy to the target material, and reduces overall energy consumption [37,38].

Extensive studies on agricultural and forestry residues demonstrate how key process variables; impregnation ratio, activation temperature, and time, govern texture and adsorption metrics in chemically (e.g., $ZnCl_2$) and physically (CO_2/steam) activated carbons. Representative examples include $ZnCl_2$-activated Elaeagnus angustifolia seeds and vetch showing strong dependence on impregnation ratio and temperature/time on iodine number and BET surface area, pistachio-shell carbons reaching $> 1100\ m^2\ g^{-1}$ under optimized $ZnCl_2$ routes, and acorn-shell carbons achieving up to $\sim 1779\ m^2\ g^{-1}$ via H_2O–CO_2 physical activation [39,40].

In the context of biochar activation, induction heating has been investigated for its ability to enable controlled chemical activation of biochar by rapidly heating metal catalysts [41]. Studies have demonstrated that induction heating can reduce activation times by up to 50 % compared to conventional methods, reaching temperatures as high as 1000°C within minutes. It has also proven effective in facilitating activation reactions between biochar's carbonaceous structure and CO_2 or H_2O (steam), enhancing pore development [42,43]. Furthermore, the contactless nature of induction heating minimizes contamination risks, providing a clean activation environment that makes it particularly appealing for high-purity applications [44].

The adaptability of induction heating to various process parameters, such as power density, heating duration, and frequency, offers significant advantages in tailoring the properties of activated carbon [45]. For instance, increased power density accelerates activation kinetics, while modulation of activation time enables precise control over porosity and surface functionality.

Induction heating-based production of activated carbon remains a relatively under-explored area in current literature. While various studies have examined biomass pyrolysis using induction heating, including catalytic upgrading to produce high-quality bio-oil with reduced oxygen content and coke formation [46], detailed investigations specifically into the activation of biochar through induction methods are scarce. Further research into induction heating-based activation of biochar, particularly focusing on catalytic influences and optimal operational parameters, is necessary to substantiate these findings and realize practical industrial applications. These prior $ZnCl_2$ and CO_2/steam-based routes delineate the conventional thermal landscape; however, they typically rely on bulk heating and long residence times. In contrast, the present work leverages induction-driven, catalyst-assisted CO_2 activation to shorten diffusion lengths and intensify interfacial gasification, building upon the textural baselines reported for $ZnCl_2$-activated Elaeagnus/vetch and CO_2-activated acorn shells [47].

Research has reported that biochar activated using higher heating pyrolysis in the presence of CO_2 at 900°C for just 15 min achieved a BET surface area of 1300 $m^2\ g^{-1}$ [27]. Experimental work revealed that incorporating 5 % Fe_2O_3 catalyst into biochar led to increase in micropore volume compared to activation with CO_2 alone. Additionally, the BET surface area improved from 800 to 1250 $m^2\ g^{-1}$, highlighting the efficacy of Fe_2O_3 in catalytic activation processes [14]. Induction heating systems typically operate at currents ranging from 300 to 600 A, with higher currents accelerating activation kinetics. Activation durations in the literature range from 30 to 90 min, with extended times generally increasing pore volume but potentially causing excessive mass loss [48–50]. Another research observed that a 60-minute activation period was sufficient to achieve high BET surface areas without compromising yield, emphasizing the versatility of this method in meeting diverse industrial and environmental demands [28].

The activation process can be further optimized by incorporating iron-based catalysts, which exhibit unique advantages in facilitating pore formation and altering surface functionalities. CO_2 is recognized as a selective oxidant that particularly promotes micropore formation [51], and compared to H_2O, it generates more controlled pore structures with higher surface areas [52]. Iron-based catalysts, when employed in conjunction with CO_2, accelerate the Boudouard reaction and facilitate carbon gasification [53]. Moreover, the localized heating effect of Fe particles under heat promotes homogeneous pore development and accelerates the reaction kinetics. Owing to this dual mechanism, increases of up to 40 % in microporosity and BET surface area have been reported relative to CO_2 activation alone [54]. When coupled with CO_2, iron-based catalysts uniquely enhance pore formation and modify surface functionalities by accelerating redox-driven carbon gasification, thereby producing activated carbons with superior microporosity and surface area compared to non-catalyzed processes. Iron-catalyzed carbons exhibit up to 40 % higher microporosity compared to uncatalyzed controls under similar activation temperatures. Additionally, localized heating effects generated by iron particles under induction accelerate reaction kinetics, leading to more uniform and finely tuned pore structures.

This study integrates induction heating with the synergistic effects of CO_2 and iron-based catalysts to produce granular activated carbon from biochar obtained by gasification using a thermal degradation method of pine pruning waste from timber-related industries. By systematically optimizing key activation parameters, the study aims to enhance the scalability and environmental sustainability of biochar activation. Detailed characterization of the resulting activated carbon, including pore structure, surface area, and functional group analysis, underscores the transformative potential of this method. Moreover, this research highlights the importance of positioning induction heating as a pivotal technology in sustainable material processing, emphasizing its role in biomass valorization and waste reduction for future advancements.

The originality of this study lies in the development of a rapid, energy-efficient activation process with enhanced porosity, achieved

through the combined use of induction heating, CO_2, and iron-based catalysts, a technique that has been scarcely addressed in the literature. This approach represents a significant innovation, offering both the valorization of biomass waste and the production of high-performance activated carbon with lower energy consumption compared to conventional pyrolysis or chemical activation methods.

2. Experimental

2.1. Preparation of biochar

The biochar was produced via the thermal degradation of pine pruning residues sourced from Lufkin, East Texas, as a by-product of the gasification process. The thermal degradation process through which the biochar was obtained was conducted in a controlled environment using a vertical, cylindrical fixed-bed reactor unit constructed with SS316 stainless steel liner, backed by a 25 mm high-alumina refractory layer to tolerate 700–900 °C operation. The hot zone had an internal diameter of ~0.30 m and a packed-bed height of ~0.85 m, corresponding to an internal free volume of ~60 L. The reactor was maintained at approximately 70–80 % volumetric loading during operation to ensure stable gas-solid contact and uniform heat distribution throughout the bed [55]. Prior to feeding, the pruned biomass was chipped and screened to median particle size d50 ≈ 15 mm, interquartile range 12–18 mm to ensure stable gas–solid hydrodynamics in the fixed-bed reactor. Fines < 8 mm were removed to mitigate channeling, and oversize > 25 mm was re-chipped. The feedstock, consisting of chipped and uniformly sized pine pruning waste, was pre-dried to a moisture content of approximately 20 % to optimize thermal efficiency during the process. This moisture level was selected based on prior studies demonstrating that moderate moisture content (15–25 %) enhances heat transfer, reduces excessive drying energy, and promotes uniform gasification without compromising biochar yield [56]. As detailed in Table 1, which presents the element composition and proximate properties of the material.

The reactor was operated within a temperature range of 700–900°C under a limited oxygen supply (under 25 kg h^{-1} nominal throughput and fuel-to-air equivalence ratio (ER) of 0.27), facilitating partial combustion and enabling the conversion of waste biomass into biochar, syngas, and tar. The process flow illustrated in Fig. 1**(a)** was carefully monitored, focusing on critical parameters such as feedstock loading rate, residence time, and gas flow rate, to ensure consistent biochar yields with optimal physicochemical properties. The biochar yield was approximately 17 % by weight under sub-stoichiometric air (ER = 0.27), corresponding to an output of 4,25 kg h^{-1} from the 25 kg h^{-1} biomass feedstock under the described operational conditions.

Table 1
Main characteristics of pine pruning waste and produced biochar.

Ultimate analysis[a]	**Pinewood Pruning**	**Biochar**
Carbon	48,32	79,76
Hydrogen	6,76	5,68
Nitrogen	0,59	1,29
Sulfur	0,07	0,16
Oxygen[c]	44,26	13,11
Proximate analysis[b]		
Ash	1,51	5,74
Volatile Matter	81,77	11,48
Fixed Carbon	16,72	82,78
HHV[c] (MJ/kg)	20,29	33,18

[a]on a dry basis
[b]As prepared (air-dried and fines free, and ground <0,5 mm)
[c]calculated according to the HHV formula [57]

2.2. Experimental setup and instrumentation

An induction heating system (TRW-10, Ilbahar Co., Ltd., Turkiye) was used for the experimental activation processes. The system operates with a power rating of 10 kW and an input voltage of 220 V, 50 Hz, supporting continuous operation with a 100 % duty cycle. Temperature control was achieved via customized induction coils paired with a pure graphite crucible and ceramic sleeve to ensure uniform heating. The equipment's oscillation frequency ranged from 28 to 40 kHz, ensuring efficient energy transfer. A cooling water system was integrated to maintain optimal operating conditions, requiring a flow rate of ≥ 20 L min^{-1} and a maximum water temperature of 40°C. Additional accessories, such as a foot pedal and tongs, facilitated precise control and sample handling.

Additionally, an activation gas inlet was integrated into the system shown in Fig. 1(b) via a custom-designed quartz tube (labeled as (5) in Fig. 1(b)) has an inner diameter of 25.4 mm and a length of 320 mm. This quartz tube was specifically engineered to seamlessly interface with the induction heater, enabling the controlled introduction of activation gases during the experiments. The quartz tube's thermal and chemical resistance ensured compatibility with the high-temperature environment and reactive gases. This setup facilitated precise control over experimental parameters, enhancing the reproducibility and ease of operation.

2.3. Experimental procedure

Biochar derived from the thermal degradation of pine pruning were subjected to drying at 105°C for 24 h under an inert nitrogen atmosphere to prevent moisture formation and ensure the removal of macroporous contaminants. Following this process, the samples were vacuum sealed to maintain their integrity, then activated under a CO_2 atmosphere in a batch induction system utilizing iron-based catalysts. Activation was conducted at four distinct current levels and durations. Each experimental condition was replicated in triplicate to ensure reproducibility.

Uniform granular biochar samples, with an average particle size of 8 mesh, were prepared and weighed into 3 g aliquots for each activation batch. Preliminary experiments were conducted to optimize the catalyst loading, testing amounts ranging from 0 to 60 g per 3 g biochar. Based on these trials, the optimized catalyst-to-biochar mass ratio was established as 15:1 (45 g catalyst per 3 g biochar), which was used consistently throughout all subsequent activation experiments (detailed results are presented in Section 3.3).

The iron-based catalyst pellets were prepared under the supervision of Gebze Technical University at the workshop of Ilbahar Co. (Türkiye) using a hydraulic pelletizing press. The catalyst composition consisted of iron powder (particle size:45–150 μm, purity ≥99.5 % Sigma-Aldrich), nickel powder (particle size: <50 μm, purity ≥99.8 %, Alfa Aesar), titanium powder (particle size: <44 μm, purity ≥99.5 %, Alfa Aesar), and graphite powder (particle size: <20 μm, purity ≥99.9 %, Merck) as carbon source. The powders were wighed according to the target composition and homogeneously mixed using a planetary ball mill at 300 rpm for 2 h under argon atmosphere to prevent oxidation. The homogenized powder mixture was then compacted into spherical pellets using a hydraulic press at 150 MPa. The pellets were subsequently sintered at 900°C for 2 h under a reducing atmosphere to enhance mechanical strength and promote alloy formation. This sintering process facilitated the formation of Fe_3C and $FeNi_3$ phases. ICP–OES analysis determined the bulk composition of the catalyst as Fe–Ni–Ti–C = 85.0–6.0–3.0–6.0 wt%. Surface analysis by XPS indicated an atomic composition of Fe:Ni:Ti:C = 88:7:3:2 at%. XRD confirmed Fe, Fe_3C, and $FeNi_3$ as the predominant crystalline phases, with minor TiC also detected. The biochar and iron-based catalyst (Fe-Ni-Ti-C) were thoroughly mixed and subsequently shaped into spherical pellets (diameter 3.0 ± 0.1 mm) to ensure homogeneity and intimate contact between the

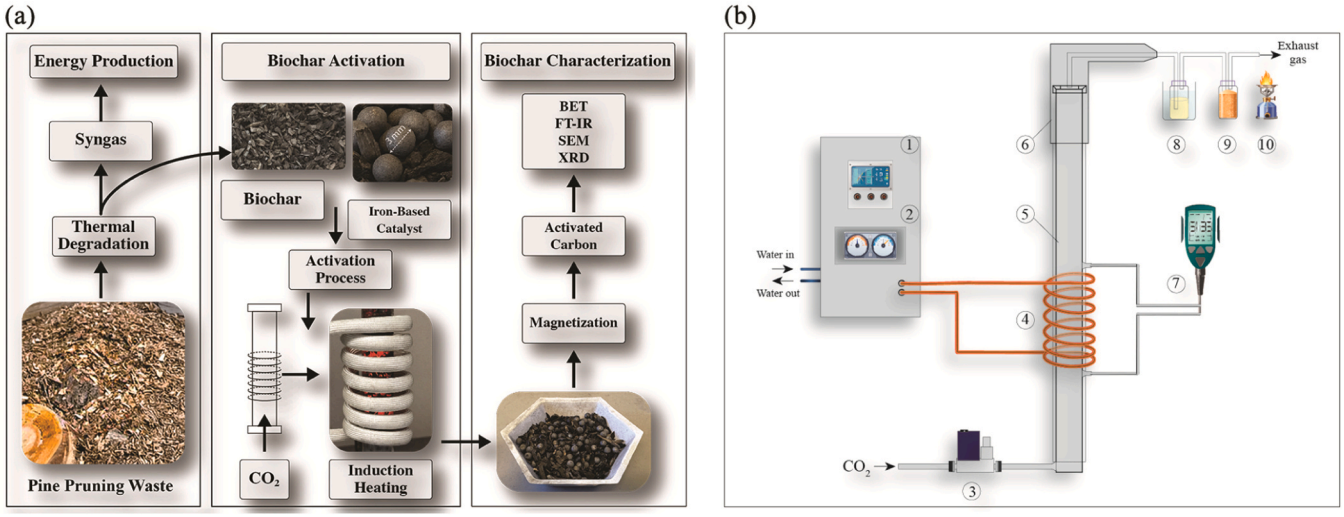

Fig. 1. (a) Valorization of pine-pruning waste: thermal degradation yielding syngas and biochar; CO_2 activation of the biochar under high-frequency induction (HFI) to obtain activated carbon. (b) Induction-assisted CO_2-activation setup: (1) HFI generator, (2) HFI controller, (3) mass-flow controller (MFC), (4) induction coil, (5) reactor tube, (6) thermal insulation, (7) thermocouple setup, (8) condenser system, (9) filter system, and (10) off-gas burner.

carbon matrix and catalyst particles. The mixtures were then placed at the center of a quartz tube housed within the induction heating coils indicated in Fig. 1**(b).** The quartz tube was connected to both gas inlet and outlet ports to facilitate controlled gas flow during the experiments.

During activation, the gas flow was maintained at a constant rate of 15 mL min^{-1} and evenly distributed using an inlet diffuser. Prior to initiating the induction system, the quartz tube was purged with CO_2 for 5 min to eliminate residual oxygen. The induction heater was subsequently operated at reaction currents of 200, 300, 400, and 500 A, with activation durations determined through preliminary tests, based on activation temperature benchmarks established in prior studies [14,26, 48–50]. Gaseous by-products generated during the activation process were evacuated and filtered via a vacuum system, then directed through an off-gas burner to ensure their complete removal from the reaction chamber.

Upon completion of the activation process, the induction heater was deactivated, and the quartz tube was allowed to cool under an inert gas flow. Once cooled, the activated biochar samples were carefully collected and separated from the iron catalysts using a magnet separator. The yield of the activation process was determined by weighing the recovered biochar residues. The activated samples were precisely packaged for further analysis.

2.4. Structural, chemical and thermal analysis

X-ray diffraction (XRD) analysis of the biochar samples was performed using a Rigaku D-MAX 2200 PCI diffractometer (Rigaku Corporation, Japan). The system employed Cu-Kα radiation and operated at a scanning rate optimized for precise phase identification and crystallite size determination. Patterns were recorded in the 2θ range of 10°–80° with a step size of 0.02° at room temperature. Fourier transform infrared (FT-IR) spectra were obtained using a PerkinElmer Spectrum 100 spectrometer (PerkinElmer, USA). The spectral data were recorded over a wavenumber range of 400–4000 cm^{-1} to identify functional groups, and chemical bonds present in the samples. All measurements were conducted at room temperature under standard atmospheric conditions. Thermal analysis of the samples was conducted using a Metter Toledo TGA/SDTA851e thermal analyzer (Mettler-Toledo, Switzerland). The heating rate was set to 20°C min^{-1}, and the analyses were carried out in a nitrogen atmosphere with a flow rate of 50 mL min^{-1} to ensure a controlled inert environment. The system provided simultaneous measurement of mass loss (TGA) and heat flow (DTA) to evaluate thermal stability and compositional changes.

2.5. Micromorphology and surface analysis

The surface morphology of pine pruning waste and the activated biochar was analyzed using a high-resolution scanning electron microscope (FEI PHILIPS XL30 SFEG, USA). The instrument operates at an adjustable accelerating voltage of 0.5–30 kV and offers magnifications up to 500,000 ×, enabling detailed imaging at the nanometer scale. Both secondary electron and backscatter electron detectors were employed to evaluate the microstructural features, surface textures, and morphological changes induced by the activation process.

The specific surface area and porosity of the samples were determined using a Micromeritics TriStar II PLUS gas adsorption analyzer (Micromeritics, USA). Nitrogen adsorption data were collected at a temperature of 77 K, and the adsorption equilibrium time was set to 90 s to ensure precise measurements. The Brunauer-Emmett-Teller (BET) method was applied to calculate the specific surface area based on nitrogen adsorption within the relative pressure range of 0.01–0.3 (p/p_o). This method provides quantitative surface area values but does not yield pore size distribution or pore volume data; such analyses require additional methods (e.g., BJH or NLDFT) which were not applied in this study. Unlike SEM, which only reveals surface morphology and larger pore openings, BET quantifies the accessible internal surface area accessible to nitrogen molecules at the nanometer scale. Thus, combination of SEM and BET analyses provided comprehensive insights into the structural and textural properties of the biochar samples, critical for assessing their suitability for targeted applications.

3. Result and discussion

3.1. TGA analysis

Thermogravimetric (TGA) and derivative thermogravimetric (DTG) curves for pine biomass pruning waste and its derived biochar are presented in Fig. 2**(a)** and Fig. 2**(b)**, respectively. Both analyses were conducted under an inert (N_2) atmosphere from ambient temperature to ~900 °C.

For the pine biomass, an early, gradual mass loss appears below ~150 °C, reflecting moisture evaporation and the release of light volatiles. The main decomposition between 200 °C and 400 °C shows a pronounced DTG peak at 355.50 °C, associated with the overlapping

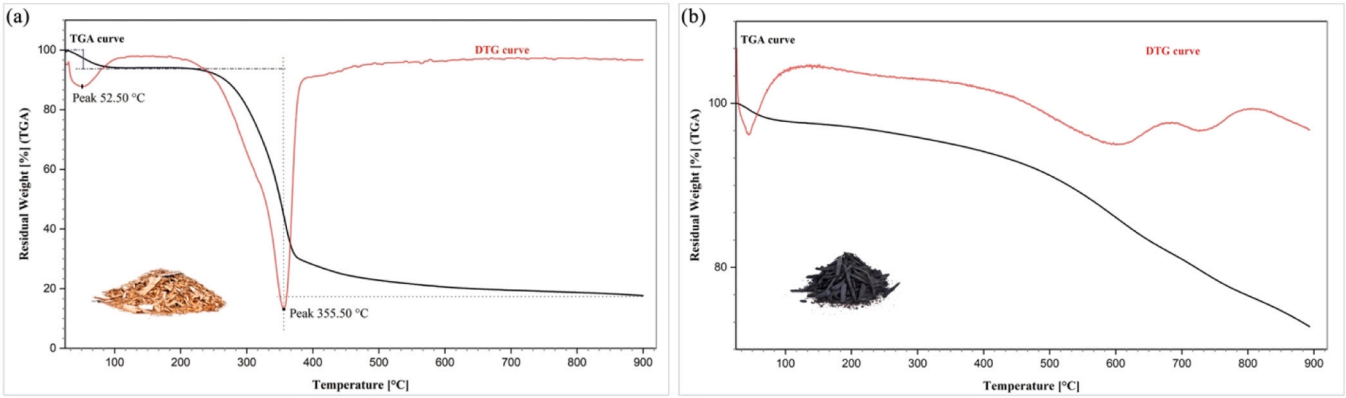

Fig. 2. (a) Thermogravimetric Analysis (TGA) Curves of Pine Biomass and (b) Its Gasification-Derived Biochar.

degradation of hemicellulose and cellulose, two major lignocellulosic components. Above 400 °C, lignin a more complex aromatic polymer decomposes slowly, resulting in a gradual reduction in mass [58,59]. By 900 °C, about 15–20 wt % remains, comprising inorganic ash and highly condensed carbonaceous residues.

In contrast, the biochar shows minimal mass loss up to ~300 °C, indicating the prior removal of most volatiles and moisture during gasification. A minor DTG peak may appear between 50 °C and 150 °C, corresponding to residual moisture or trace volatiles. From 300 °C to 600 °C, the biochar's mass loss is modest and gradual, reflecting a thermally stable carbon matrix that undergoes only limited further decomposition of residual organics [60,61]. Above 600 °C, the biochar exhibits high thermal stability and retains a substantial fraction of mass at 900 °C, predominantly as fixed carbon and ash.

Overall, these TGA profiles confirm that thermal gasification effectively removes volatiles from pine biomass, yielding a carbon-rich biochar with enhanced thermal stability and a higher final residue. The biochar's limited mass loss across the entire heating range underscores its suitability for applications demanding robust thermal and structural properties, including activated carbon production.

3.2. *Effect of activation time on mass loss and surface area development*

The data obtained from this study reveal a strong correlation between mass loss and surface area in CO_2-induced induction activation. While increasing current intensity and activation time enhances pore development, it also results in mass loss. Therefore, to achieve activated carbon with desired properties, both current intensity (and, by extension, temperature) and activation duration must be carefully optimized to strike a balance between pore structure enhancement and material yield.

Table 2
Induction Activation Parameters and Resulting Yield/BET Surface Area for Pine Pruning Biochar.

Current (A)	Time (min)	Output (g)	Yield (%) *	Mass Loss (%)*	BET (m^2 g^{-1})
200	30	2.59	86.3	13.7	607.21
300	30	2.32	77.3	22.7	630.39
400	30	1.58	52.7	47.3	749.23
500	30	1.37	45.7	54.3	768.49
200	60	2.14	71.3	28.7	620.64
300	60	1.99	66.3	33.7	693.45
400	60	1.35	45	55	805.72
500	60	0.61	20.3	79.7	865.07
200	90	2.07	69	31	634.05
300	90	1.94	64.7	35.3	698.45
400	90	1.45	48.3	51.7	801.82
500	90	0.48	16	84	854.65

* Percentages calculated based on initial 3 g of biochar.

A detailed examination of Table 2 reveals that during induction-assisted activation in the presence of CO_2 and iron-based catalysts, mass loss increases significantly with both higher applied current (amperes) and activation duration (minutes). In the experiments, all samples were initially weighed at 3 grams, and the final product mass was measured after activation to calculate the extent of mass loss.

Examining the effect of time under a constant current revealed that mass loss was directly proportional to activation duration. At 200 A, for instance, the mass loss rose from approximately 13.7 % after 30 min to 28.7 % after 60 min, and further to 31 % after 90 min. A similar pattern emerged at 300 A, where the loss increased from 22.7 % after 30 min to 35.3 % after 90 min. Additionally, increasing the current at a fixed activation time also had a pronounced effect: after 30 min of activation, mass loss climbed from 13.7 % at 200 A to 54.3 % at 500 A. The most dramatic result occurred at 500 A over 90 min, reaching an approximately 84 % loss of the initial mass. Under CO_2 flow and in the presence of catalysts, elevated temperature (indirectly set by current intensity) and prolonged exposure time accelerated carbon gasification, promoting pore formation and thereby leading to greater pore volume and surface area. Indeed, as shown in the table, heightened activation intensity and duration correlated with a substantial rise in BET surface area of the material. For example, in 30-minute activations, BET values increased from 607.21 m^2 g^{-1} at 200 A to 768.49 m^2 g^{-1} at 500 A; over 60 min, they climbed from 620.64 m^2 g^{-1} at 200 A to 865.07 m^2 g^{-1} at 500 A.

The relationships presented in Table 2 are summarized visually in Fig. 3**(a)**, where BET surface area and product yield are mapped to height and color, respectively, providing an integrated representation of four interrelated variables. Several notable insights emerge: A coupled optimization region appears as a shallow ridge of elevated BET values (≈820–880 m^2 g^{-1}) at currents between 400–500 A and activation times of 60–70 min. However, this ridge gradually shifts from green to indigo, reflecting a concurrent drop in yield below 40 %. Conversely, a distinct yellow-green region at lower conditions (200–300 A and 40–50 min) maintains high yields (>70 %) but achieves only moderate BET values (≈630–700 m^2 g^{-1}). This clearly illustrates the practical trade-off between "surface-area-driven" and "yield-driven" operational regimes, with micropore volumes ranging from 0.28 to 0.35 cm^3 g^{-1} and increasing mesopore contributions at higher activation intensities. A nonlinear current effect is also evident, with surface curvature steepening markedly beyond ≈ 400 A, indicating diminishing returns in BET enhancement accompanied by disproportionately larger losses in yield. This behavior aligns with thermokinetic considerations, suggesting that beyond a critical catalyst temperature, additional current preferentially accelerates carbon gasification rather than forming new porosity. Additionally, a plateau in time sensitivity emerges at lower currents (≤300 A) after approximately 60 min, where further activation contributes minimally to BET surface area but results in an additional yield reduction of 3–5 %. This plateau points to CO_2 diffusion limitation at

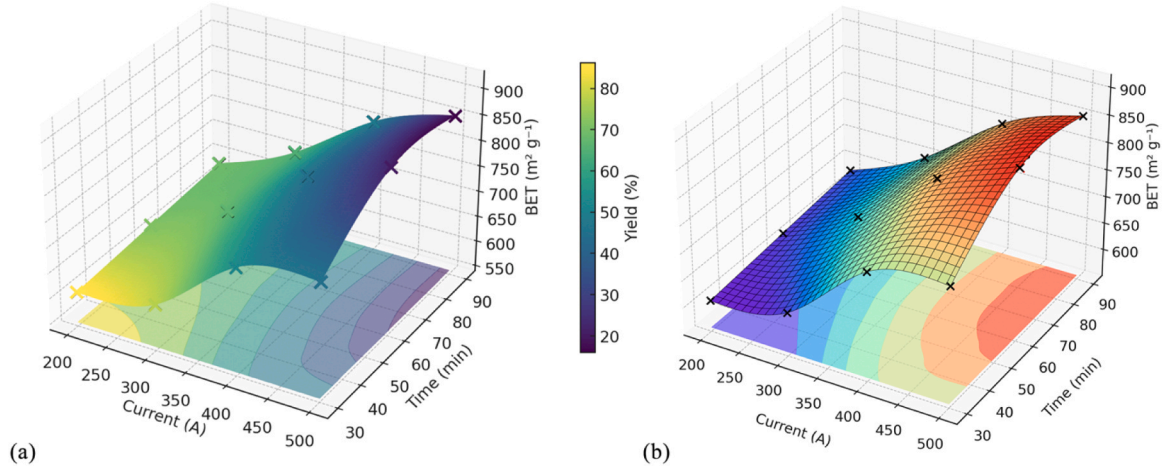

Fig. 3. (a) 3D response surface of BET surface area ($m^2\ g^{-1}$) vs. current (A) and activation time (min), colored by Yield (%). (b) Same 3D surface, colored by BET surface area ($m^2\ g^{-1}$).

reaction sites under lower-temperature conditions. Overall, Fig. 3**(a)** confirms and visually enhances the numerical insights from Table 2, clearly defining the multi-objective landscape and underscoring that the optimal balance between BET surface area and yield occurs near 350–400 A and approximately 60 min activation time, where BET surface area exceeds 750 $m^2\ g^{-1}$ and yields remain above 50 %. These findings corroborate previous observations that higher currents intensify localized heating within iron catalyst regions, thereby accelerating the Boudouard reaction under CO_2 flow [62]. This increased reaction rate induces significant structural transformations within the carbon matrix. Similarly, extended activation durations prolong reaction interactions, further altering the biochar structure. While higher currents and longer durations partially enhance pore development, the combined effect of prolonged exposure to high currents and extended durations reduces overall yield and leads to the breakdown of microporous structures, ultimately resulting in a decline in surface area.

These findings align well with recent literature on CO_2-activated biochar. For instance, Menegazzo et al. [63] reported BET surface areas of 520–600 $m^2\ g^{-1}$ for walnut shell biochar activated at 800–900°C under CO_2, with yields of 35–55 %, which are comparable to our moderate activation conditions (300–400 A, 60 min: 693–805 $m^2\ g^{-1}$, 45–66 % yield). Plaza et al. [64] achieved 720 $m^2\ g^{-1}$ for pine-derived biochar using conventional CO_2 activation at 800°C for 30 min, but with significantly lower yields (~30 %). In contrast, studies employing chemical activation (KOH, H_3PO_4) typically report higher surface areas (1000–1500 $m^2\ g^{-1}$) but require extensive washing and generate chemical waste [65]. Our approach achieves competitive surface areas (up to 865 $m^2\ g^{-1}$) with cleaner CO_2-based physical activation, enhanced by iron catalysis and rapid induction heating.

3.3. Effect of catalyst

The role of the iron-based catalyst in the induction heating activation process was systematically investigated through preliminary experiments conducted at 400 A with varying catalyst loadings (0–60 g) per 3 g biochar. These experiments revealed that the catalyst serves a dual function: (i) as a susceptor material that converts electromagnetic energy into localized heat through hysterisis and eddy current losses in ferromagnetic phases (Fe, $FeNi_3$), and (ii) as a potential catalytic agent that may facilitate the Boudouard reaction ($C + CO_2 \rightarrow 2CO$) at the metal-carbon interface [66–68]. Under catalyst-free conditions, no detectable heating occurred during induction, and the biochar surface area remained essentially unchanged at 47.38 $m^2\ g^{-1}$, confirming that the presence of ferromagnetic material is essential for energy coupling in this system. Pore development became evident only above 10 g of catalyst loading. At 400 A, the BET surface area reached approximately 200 $m^2\ g^{-1}$ with 15 g of catalyst, increased to ~400 $m^2\ g^{-1}$ with 25 g, and further improved to ~600 $m^2\ g^{-1}$ with 35 g. However, beyond 45 g, no significant further improvement was observed in either pore volume or BET surface area, indicating that the system had reached a saturation point where additional catalyst did not enhance heat generation or gasification efficiency. The maximum pore development was consistently achieved at 45 g, corresponding to catalyst-to-biochar mass ratio of 15:1, which was therefore adopted as the optimized loading for all subsequent experiments.

The observed saturation behavior can be attributed to several factors. First, at high catalyst loadings, the biochar-catalyst samples may experience uneven heat distribution, with the outer catalyst layers shielding the inner biochar from effective CO_2 diffusion [69]. Second, excessive catalyst may dilute the biochar concentration within the pellet, reducing the effective carbon-CO_2 contact area [65]. Third, the induction coil's electromagnetic field penetration depth (skin depth) is limited, and beyond a certain catalyst thickness, additional material does not contribute to further heating.

It should be emphasized that distinguishing between the purely thermal (induction heating) and potentially catalytic (reaction enhancement) roles of iron requires comparative studies using conventional heating methods with and without catalyst, as well as detailed kinetic analysis through techniques such as TGA under CO_2 atmosphere. Such investigations fall beyond the scope of this initial experimental study but represent important directions for future work. The present results demonstrate that induction based activation is technically viable and that a 15:1 catalyst-to-biochar ratio provides a practical operating point for this novel activation approach.

3.4. Effect of electrical current

Induction-assisted activation carried out at current intensities ranging from 200 to 500 A, corresponding to manually measured temperatures of approximately 700–1100 °C, played a crucial role in determining the porosity, BET surface area, and material retention in the resulting activated carbon. As current intensity increased in the presence of an iron catalyst, carbon gasification reactions primarily via the Boudouard mechanism under flowing CO_2 significantly accelerated, raising the BET surface area from 607 $m^2\ g^{-1}$ at 200 A to 768 $m^2\ g^{-1}$ at 500 A within just 30 min. Fig. 3**(b)** illustrates this relationship by presenting BET surface area as a three-dimensional response surface dependent on current intensity and activation time, complemented by contour shading on the base plane that highlights BET gradients; notably, the steep gradient observed along the current axis underscores the dominant

influence of electrical input rather than activation time on initial pore formation. Conversely, the wider spacing between contour lines at longer durations indicates diminishing returns in BET surface area beyond approximately 60 min. The black × symbols marking experimental data points closely align with the interpolated response surface, lending strong credibility to the fitted trend. While higher currents indeed expanded the pore network, they simultaneously accelerated catalytic gasification, as evident from the observed mass losses: residual solid mass dropped from 2.59 g (a 13.7 % loss) at 200 A to 1.37 g (a 54.3 % loss) at 500 A over the same 30-minute activation period, with even more pronounced losses at activation times of 60 and 90 min. Given the strong induction–catalyst coupling, local heating and transient behavior merit a separate, targeted investigation; to maintain focus, we document the operating range (45 g: 700–1100 °C) and leave detailed kinetic dissection to future studies.

Consequently, although aggressive activation conditions may be desirable for applications demanding maximum surface area, the associated yield reduction and elevated energy consumption advocate for more moderate operating conditions, around 350–400 A for approximately 60 min, where BET surface areas surpass 750 $m^2\ g^{-1}$ and over half of the initial mass is retained, achieving a practical compromise between adsorption performance and process economy.

3.5. XRD analysis

The XRD patterns of the unactivated biochar and selected activated samples, presented in Fig. 4**(a)**, exhibited broad diffraction peaks centered around $2\theta = 20°–25°$, indicative of amorphous carbon structures. Upon activation, minor peaks attributable to iron oxides (e.g., Fe_3O_4) emerged, suggesting partial oxidation of the iron catalysts during the induction heating.

Unactivated biochar showed a predominantly amorphous carbon matrix, whereas activated biochar displayed increased crystallite order in the carbon structure and identifiable peaks for Fe-oxides, underscoring the active role of iron in catalytic gasification [70,71].

The emergence of iron oxide peaks is consistent with the redox cycles described in prior literature, where iron species transition between Fe (0), FeO, and Fe_3O_4 under CO_2 activation environments [13]. These redox transitions promote carbon gasification, explaining the higher surface area and pore development measured in the activated samples. Nonetheless, controlling the oxidation state of the iron catalysts could further tailor the final carbon structure.

3.6. Activation mechanism under CO_2 and iron-based catalysis

During CO_2 activation, carbon atoms at defective sites react via the Boudouard pathway ($C + CO_2 \rightarrow 2CO$), progressively enlarging pre-existing pores [53,62]. In the presence of iron-containing nanoparticles (Fe/Fe_3C and $FeNi_3$), CO_2 is more effectively activated: oxygen species generated on metal surfaces spill over to adjacent carbon sites, forming C(O)* intermediates that desorb as CO [13,53]. Concurrently, a carbide cycle operates, where Fe transiently forms Fe_3C at locally hot metal-carbon interfaces and subsequently decarbides under CO_2/CO, thereby renewing reactive interfacial sites. A complementary $FeO_x \leftrightarrow Fe$ redox shuttle may also transfer oxygen to carbon under CO-rich conditions.

Induction heating intensifies these pathways by selectively heating ferromagnetic phases ($Fe/FeNi_3$), creating local temperature gradients that nucleate pores at the metal–carbon interface and accelerate gasification kinetics without excessive global burn-off [72]. As a result, the synergy of CO_2 with iron-based catalysts yields earlier-onset and more homogeneous micropore development, followed by controlled mesopore widening, while enriching the surface with oxygen-containing functional groups that enhance adsorption affinity.

3.7. FTIR analysis

FTIR spectral analysis of pine pruning biomass, its biochar, and activated biochar reveals significant chemical transformations during thermal degradation and subsequent induction activation. In the raw pine biomass, Fig. 4**(b)** shows a broad O-H stretching band centered around 3300–3400 cm^{-1}, which indicates hydrogen-bonded hydroxyl groups in cellulose, hemicellulose, and lignin. Prominent C-H stretching vibrations near 2920 and 2850 cm^{-1} suggest the presence of aliphatic $-CH_2$ and $-CH_3$ groups, while a distinct peak at about 1730 cm^{-1} arises from C═O stretching in unconjugated carbonyl groups, likely associated with ester and carboxyl functionalities in hemicellulose or extractives. Additionally, peaks near 1600 cm^{-1} and 1510 cm^{-1} are attributed to aromatic skeletal vibrations of lignin, and an intense band around 1030 cm^{-1} in the fingerprint region reflects C-O stretching and C-O-C linkages in cellulose and hemicellulose. These features confirm that the biomass contains abundant hydroxyl, aliphatic, and oxygenated functional groups characteristic of lignocellulosic materials [73–75].

When the biomass is gasified to produce biochar, the FTIR spectrum undergoes marked changes. The broad O-H band is greatly diminished, reflecting the loss of free and hydrogen-bonded hydroxyl groups due to dehydration and devolatilization. The aliphatic C-H bands nearly disappear, indicating the breakdown of hydrocarbon chains from cellulose and hemicellulose, and the prominent carbonyl peak at 1730 cm^{-1} vanishes as ester and carbonyl groups are cleaved or volatilized [76,77]. In contrast, a broad absorption band emerging around 1580–1600 cm^{-1} indicates the formation of fused aromatic rings and polyaromatic domains: the original discrete lignin peaks merge into this broader feature, signifying the conversion of distinct aromatic units into a consolidated network. The substantial reduction of bands between 1200 and 1000 cm^{-1} further confirms the decomposition of carbohydrate structures, while a weak band near 1700 cm^{-1} suggests the formation of conjugated carbonyl groups, possibly due to aromatic ketones or quinones forming on the char surface [78].

Induction activation of the biochar to yield leads to additional

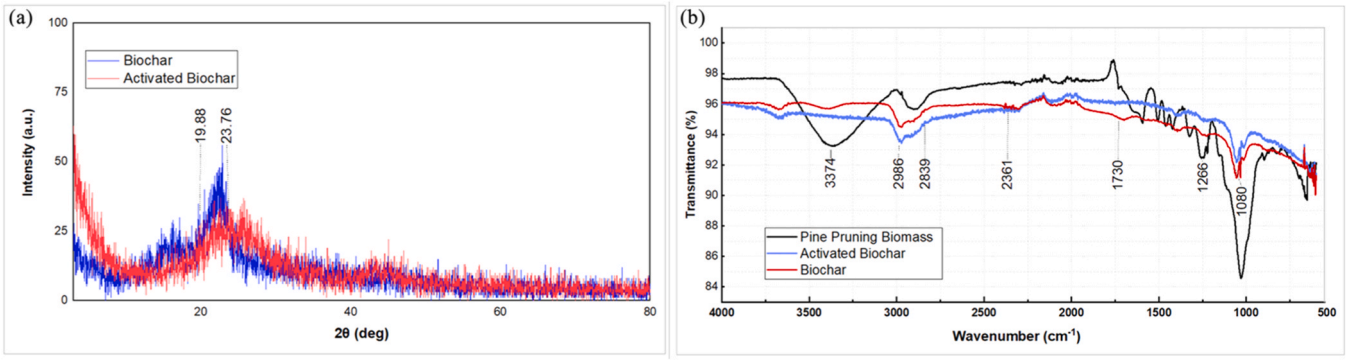

Fig. 4. (a) XRD Patterns of Unactivated and Activated Pine Pruning Biochar. (b) FTIR Spectra of Pine Pruning Biomass, Biochar, and Activated Biochar.

modifications that highlight oxidative re-functionalization of the carbon surface. In the activated biochar, the O-H stretching band near 3400 cm^{-1} becomes more pronounced, indicating an increased presence of hydroxyl groups such as phenolic -OH or adsorbed water introduced during activation. A strong C═O stretching band reappears in the 1700–1720 cm^{-1} region, pointing to the formation of new carbonyl-containing groups such as carboxylic acids, lactones, and ketones. Although the dominant aromatic C═C band around 1580 cm^{-1} remains, its relative intensity is slightly reduced, suggesting that some aromatic rings may have been oxidatively modified [79,80]. Moreover, the fingerprint region now displays a broadened and intensified envelope between 1200 and 1000 cm^{-1}, which can be attributed to C-O stretching vibrations from a variety of oxygenated groups, including alcohols, phenols, ethers, and carboxylates [81].

Overall, the FTIR spectral data clearly demonstrate the chemical evolution from raw pine biomass to biochar and finally to activated biochar. The initial material, rich in hydroxyl, aliphatic, and carbonyl functionalities, is transformed during pyrolysis into a carbon-rich, aromatic structure with diminished oxygenated groups, and subsequent activation reintroduces polar functionalities onto the stable aromatic framework.

3.8. Morphological analysis

The SEM images illustrate the morphological evolution of pine pruning waste biochar before and after induction heating activation at an induction current range of approximately 200–500 A, as shown in Fig. 5 Initially, the raw pine pruning waste exhibits a compact and orderly cellular structure, clearly visible in subfigures (a–d). The intact, elongated cell walls and defined pores indicate a relatively dense and rigid biomass matrix, typical of untreated lignocellulosic material. At higher magnifications (subfigures c and d), the surface appears relatively smooth, with minimal disruptions or microstructural defects. Following activation via induction heating, substantial morphological transformations become apparent (subfigures e–h). The thermal and catalytic action during activation drastically alters the structural integrity of the biomass, leading to significant surface disruption and pore development. Subfigures (e) and (f) depict the emergence of pronounced pore structures and increased surface roughness, indicative of successful activation. Moreover, the orderly arrangement seen in raw materials gives way to irregular, fragmented, and porous networks, a characteristic outcome of high-temperature thermal treatment in CO_2 environments.

At even higher magnifications (subfigures g and h), the activated samples demonstrate markedly enhanced surface roughness and complex pore networks. The surfaces are now extensively etched, highlighting substantial microporosity and mesoporosity. Such morphological characteristics are particularly beneficial for activated carbon applications, as they correlate strongly with increased surface areas and adsorption capacities. In summary, induction heating activation at an induction current range of approximately 200–500 A profoundly transforms the pine pruning waste structure from a dense, ordered configuration to a highly porous and irregularly textured morphology. It should be noted that SEM imaging provides only qualitative morphological insights, such as surface roughness, pore openings, and structural collapse. In contrast, BET analysis quantifies the internal surface area at the nanometer scale. However, BET alone does not provide pore size distribution or pore volume; such data require additional analyses (e.g., BJH or NLDFT methods), which were not performed in this study. Therefore, while SEM confirms the formation of pores and surface etching, BET quantifies only the accessible surface area. These structural alterations are instrumental in enhancing the activated carbon's functional properties, making it particularly suitable for various industrial and environmental applications.

4. Conclusion

This study demonstrates the effectiveness of induction heating coupled with CO_2 and iron-based catalytic activation in transforming pine pruning waste biochar into high-quality activated carbon. Comprehensive characterization through TGA, BET, FTIR, XRD, and SEM analyses confirmed significant enhancements in both porosity and surface chemistry. Under optimal conditions (500 A, 60 min, catalyst-to-biochar ratio 15:1), the BET surface area of 865.07 $m^2\ g^{-1}$, representing a marked improvement from the initial 47.38 $m^2\ g^{-1}$. However, this substantial porosity enhancement was accompanied by considerable mass loss (up to 84.7 % at the most severe conditions), emphasizing the need to carefully balance activation parameters to optimize both yield and quality.

The results underscore the synergistic effects of CO_2 and iron-based catalysts under induction heating; CO_2 acts as an oxidizing agent for the carbon matrix, while the iron-based material serves as a susceptor for electromagnetic to thermal energy conversion, enabling rapid localized heating that enhances gasification kinetics and pore development. This approach offers notable advancement over conventional pyrolytic or chemical activation methods, including dramatically reduced processing times and potential energy efficiency benefits. The methodology presents a promising sustainable strategy for valorizing agricultural waste into activated carbon suitable for diverse environmental and industrial applications.

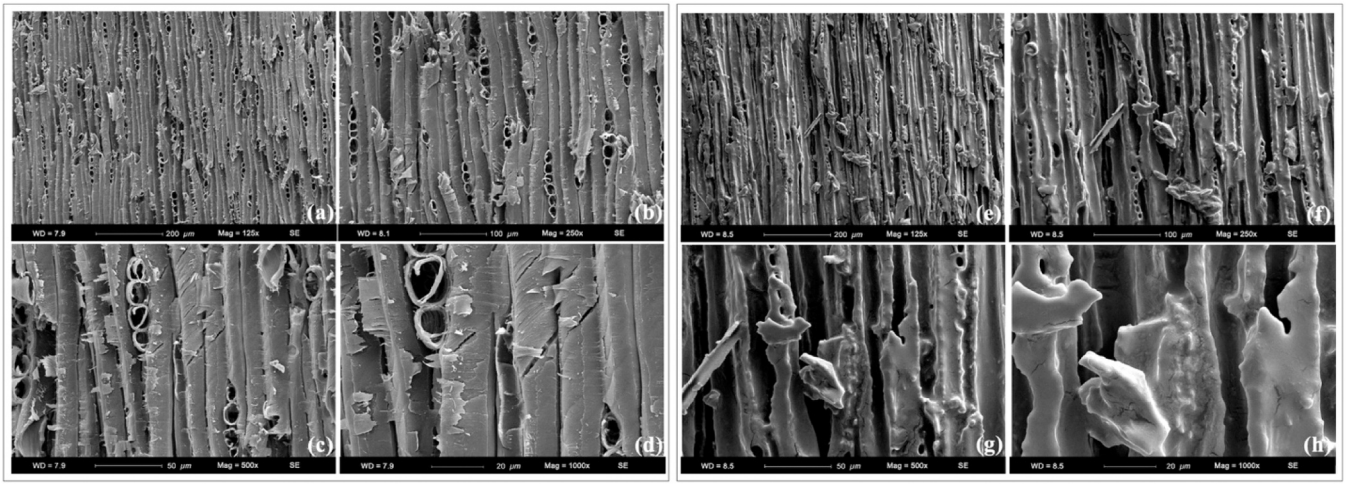

Fig. 5. SEM micrographs showing morphological changes of pine pruning waste and derived activated carbon samples before and after induction heating activation.

While this study successfully establishes the technical feasibility and optimization of induction-based activation, important questions remain regarding the fundamental mechanisms. Specifically, distinguishing between the purely thermal (susceptor-mediated heating) and potentially catalytic roles of iron requires dedicated investigation through comparative studies using conventional heating with and without catalyst, detailed kinetic analysis via TGA under CO_2 atmosphere, systematic temperature profiling, and techno-economic feasibility assessment. The induction–catalyst thermal coupling and reaction kinetics constitute a complex mechanism deserving separate, comprehensive investigation.

CRediT authorship contribution statement

Muthanna H. Al-Dahhan: Writing – review & editing, Supervision, Project administration, Methodology. **Erdem Ahmet:** Writing – original draft, Visualization, Validation, Supervision, Methodology, Investigation, Data curation, Conceptualization. **Ahmed Jasim:** Writing – review & editing, Formal analysis.

Declaration of Competing Interest

The authors declare that they have no known competing financial interests or personal relationships that could have appeared to influence the work reported in this paper.

Acnowledgments

Grateful acknowledgment is made to The Scientific and Technological Research Council of Türkiye (TUBITAK) for the support through the 2219 Research Program. Special thanks are extended to the Multiphase Flows and Reactors Engineering and Education Laboratory (mFReel), the Linda and Bipin Doshi Department of Chemical and Biochemical Engineering, and the Department of Mining and Nuclear Engineering at Missouri University of Science and Technology for providing facilities, resources, and a collaborative research environment that greatly contributed to this work.

Data Availability

No data was used for the research described in the article.

References

[1] R. Devi, V. Kumar, S. Kumar, M. Bulla, A. Jatrana, R. Rani, A.K. Mishra, P. Singh, Recent advancement in biomass-derived activated carbon for waste water treatment, energy storage, and gas purification: a review, J. Mater. Sci. 58 (2023) 12119–12142, https://doi.org/10.1007/s10853-023-08773-0.

[2] R.O. Gembo, S. Odisitse, C.K. King'ondu, Transforming waste resources into efficient activated carbon for energy storage and environmental remediation: a comprehensive review, Int. J. Environ. Sci. Technol. 21 (2024) 6167–6206, https://doi.org/10.1007/s13762-024-05457-3.

[3] J. Díaz-Terán, Porosity and adsorption properties of an activated charcoal, 188, Colloids Surf. A Physicochem. Eng. Asp. 187 (1-3) (2001) 167–175, https://doi.org/10.1016/s0927-7757(01)00622-7.

[4] B.S. Girgis, S.S. Yunis, A.M. Soliman, Characteristics of activated carbon from peanut hulls in relation to conditions of preparation, Mater. Lett. 57 (1) (2002) 164–172, https://doi.org/10.1016/s0167-577x(02)00724-3.

[5] P. Treeweranuwat, P. Boonyoung, M. Chareonpanich, K. Nueangnoraj, Role of nitrogen on the porosity, surface, and electrochemical characteristics of activated carbon, ACS Omega 5 (4) (2020) 1911–1918, https://doi.org/10.1021/acsomega.9b03586.

[6] R.H. Hesas, W.M.A.W. Daud, J. Sahu, A. Arami–Niya, The effects of a microwave heating method on the production of activated carbon from agricultural waste: a review, J. Anal. Appl. Pyrolysis 100 (2013) 1–11, https://doi.org/10.1016/j.jaap.2012.12.019.

[7] Z. Heidarinejad, M.H. Dehghani, M. Heidari, G. Javedan, I. Ali, M. Sillanpää, Methods for preparation and activation of activated carbon: a review, Environ. Chem. Lett. 18 (2020) 393–415, https://doi.org/10.1007/s10311-019-00955-0.

[8] S.J. Allen, L.J. Whitten, G. McKay, The production and characterisation of activated carbons: a review, Dev. Chem. Eng. Miner. Process. 6 (5) (1998) 231–261, https://doi.org/10.1002/apj.5500060501.

[9] U. Arena, M.L. Mastellone, F. Perugini, The environmental performance of alternative solid waste management options: a life cycle assessment study, Chem. Eng. J. 96 (1-3) (2003) 207–222, https://doi.org/10.1016/j.cej.2003.08.019.

[10] Y.X. Gan, Activated carbon from biomass sustainable sources, C 7 (2) (2021) 39, https://doi.org/10.3390/c7020039.

[11] Mohd Adib Yahya, Z. Al-Qodah, C.W. Zanariah Ngah, Agricultural bio-waste materials as potential sustainable precursors used for activated carbon production: a review, Renew. Sustain. Energy Rev. 46 (2015) 218–235, https://doi.org/10.1016/j.rser.2015.02.051.

[12] J. Serafin, B. Dziejarski, X. Vendrell, K. Kiełbasa, B. Michalkiewicz, Biomass waste fern leaves as a material for a sustainable method of activated carbon production for CO2 capture, Biomass.. Bioenergy 175 (2023) 106880, https://doi.org/10.1016/j.biombioe.2023.106880.

[13] J. Lu, Q. Lu, L. Di, Y. Zhou, Y. Zhou, Iron-based biochar as efficient persulfate activation catalyst for emerging pollutants removal: a review, Chin. Chem. Lett. 34 (11) (2023) 108357, https://doi.org/10.1016/j.cclet.2023.108357.

[14] H. Liu, C. Ye, Y. Xu, Q. Wang, Effect of activation conditions and iron loading content on the catalytic cracking of toluene by biochar, Energy 247 (2022) 123409, https://doi.org/10.1016/j.energy.2022.123409.

[15] J. Guo, Y. Zhang, J. Fang, Z. Ma, C. Li, M. Yan, N. Qiao, Y. Liu, M. Bian, Reduction and reuse of forestry and agricultural bio-waste through innovative green utilization approaches: a review, Forests 15 (8) (2024) 1372, https://doi.org/10.3390/f15081372.

[16] M.J. Aliaño–González, J. Gabaston, V. Ortiz-Somovilla, E. Cantos-Villar, Wood waste from fruit trees: biomolecules and their applications in agri-food industry, Biomolecules 12 (2) (2022) 238, https://doi.org/10.3390/biom12020238.

[17] F.L. Braghiroli, L. Passarini, Valorization of biomass residues from forest operations and wood manufacturing presents a wide range of sustainable and innovative possibilities, Curr. For. Rep. 6 (2020) 172–183, https://doi.org/10.1007/s40725-020-00112-9.

[18] A.A. Ceyhan, Ö. Şahĩn, O. Baytar, C. Saka, Surface and porous characterization of activated carbon prepared from pyrolysis of biomass by two-stage procedure at low activation temperature and it's the adsorption of iodine, J. Anal. Appl. Pyrolysis 104 (2013) 378–383, https://doi.org/10.1016/j.jaap.2013.06.009.

[19] M. Kaya, Ö. Şahĩn, C. Saka, Preparation and tg/dtg, ft-ir, sem, bet surface area, iodine number and methylene blue number analysis of activated carbon from pistachio shells by chemical activation, Int. J. Chem. React. Eng. 16 (2) (2017), https://doi.org/10.1515/ijcre-2017-0060.

[20] R. Picchio, N.D. Marzio, L. Cozzolino, R. Venanzi, W. Stefanoni, L. Bianchini, L. Pari, F. Latterini, Pellet production from pruning and alternative forest biomass: a review of the most recent research findings, 2023, Materials 16 (13) (2023) 4689, https://doi.org/10.3390/ma16134689.

[21] B.P. Oswald, M.J. Bieirle, H.M. Williams, K.W. Farrish, Response of east texas mid-rotation loblolly pine plantations to poultry litter and chemical fertilizer amendments, Agric. Fac. Publ. For. Res. Open Access 06 (02) (2017), https://doi.org/10.4172/2168-9776.1000205.

[22] W.T. Chambers, Divisions of the pine forest belt of East Texas, Econ. Geogr. 6 (1) (1930) 94, https://doi.org/10.2307/140640.

[23] T.G. Ambaye, R. Djellabi, M. Vaccari, S. Prasad, T.M. Aminabhavi, S. Rtimi, Emerging technologies and sustainable strategies for municipal solid waste valorization: challenges of circular economy implementation, J. Clean. Prod. 423 (2023) 138708, https://doi.org/10.1016/j.jclepro.2023.138708.

[24] R. Kapoor, P. Ghosh, M. Kumar, S. Sengupta, A. Gupta, S.S. Kumar, V. Vijay, V. Kumar, V.K. Vijay, D. Pant, Valorization of agricultural waste for biogas based circular economy in india: a research outlook, Bioresour. Technol. 304 (2020) 123036, https://doi.org/10.1016/j.biortech.2020.123036.

[25] A. Papageorgiou, R. Sinha, E. Azzi, C. Sundberg, A. Enell, The Role of Biochar Systems in the Circular Economy: Biomass Waste Valorization and Soil Remediation. The Circular Economy - Recent Advances in Sustainable Waste Management, IntechOpen, 2022, https://doi.org/10.5772/intechopen.104389.

[26] A. Colomba, F. Berruti, C. Briens, Model for the physical activation of biochar to activated carbon, J. Anal. Appl. Pyrolysis 168 (2022) 105769, https://doi.org/10.1016/j.jaap.2022.105769.

[27] B. Sajjadi, W. Chen, N.O. Egiebor, A comprehensive review on physical activation of biochar for energy and environmental applications, Rev. Chem. Eng. 35 (6) (2019) 735–776, https://doi.org/10.1515/revce-2017-0113.

[28] H. Yi, K. Nakabayashi, S. Yoon, J. Miyawaki, Pressurized physical activation: a simple production method for activated carbon with a highly developed pore structure, Carbon 183 (2021) 735–742, https://doi.org/10.1016/j.carbon.2021.07.061.

[29] P. Vishnuram, R. Gunabalan, T.S. Babu, B. Nastasi, Induction heating in domestic cooking and industrial melting applications: a systematic review on modelling, converter topologies and control schemes, Energies 14 (20) (2021) 6634, https://doi.org/10.3390/en14206634.

[30] S.S. Patil, A.M. Kisiela-Czajka, H.P. Dasari, From non-renewable waste to activated carbon: a smart move towards sustainable development and environmental protection in a circular economy, Waste Manag. 203 (2025) 114878, https://doi.org/10.1016/j.wasman.2025.114878.

[31] R. Bamidele, M. Marszewski, Carbonization and activation of lignocellulosic biomass in liquid phase at sub-200 °c temperatures, ACS Sustain. Chem. Eng. 13 (7) (2025) 3010–3021, https://doi.org/10.1021/acssuschemeng.4c10385.

[32] A. Adán-Más, L. Alcaraz, P. Arévalo-Cid, F.A. López-Gómez, M. Montemor, Coffee-derived activated carbon from second biowaste for supercapacitor applications, Waste Manag. 120 (2021) 280–289, https://doi.org/10.1016/j.wasman.2020.11.043.

[33] W. Li, J. Peng, L. Zhang, K. Yang, H. Xia, S. Zhang, S. Guo, Preparation of activated carbon from coconut shell chars in pilot-scale microwave heating equipment at 60kw, Waste Manag. 29 (2) (2009) 756–760, https://doi.org/10.1016/j.wasman.2008.03.004.
[34] J. Fan, P.S. Shuttleworth, M. Gronnow, S.W. Breeden, J.H. Clark, D.J. Macquarrie, V.L. Budarin, Influence of density on microwave pyrolysis of cellulose, ACS Sustain. Chem. Eng. 6 (3) (2018) 2916–2920, https://doi.org/10.1021/acssuschemeng.8b00280.
[35] P. Vishnuram, R. Gunabalan, S. Ramasamy, S. Dayalan, A comprehensive overview of power converter topologies for induction heating applications, Int. Trans. Electr. Energy Syst. 30 (10) (2020), https://doi.org/10.1002/2050-7038.12554.
[36] K. Kumar, S. Dixit, M.Z. u Haq, K.M. Vafaeva, N. Vatin, M. Rekha, V.K. Awaar, S. Jhade, Revolutionizing heat treatment: novel strategies for augmented performance and sustainability, E3S Web Conf. 430 (2023) 01200, https://doi.org/10.1051/e3sconf/202343001200.
[37] I. Tunc, B.D. Karahan, O. Keles, Biomass-derived SiOx/C nanocomposite anode synthesis by induction heating for lithium ion battery, Appl. Phys. A 130 (2024) 677, https://doi.org/10.1007/s00339-024-07841-9.
[38] C.L. Roman, J. Lucas, J.A. Dorman, K.M. Dooley, Improved performance of catalysts containing pt, pt–sn, and v in the dehydrogenation of n-butane by radio-frequency induction heating, ACS Sustain. Chem. Eng. 13 (7) (2025) 2978–2997, https://doi.org/10.1021/acssuschemeng.4c10045.
[39] A.A. Ceyhan, Ö. Şahîn, O. Baytar, C. Saka, Surface and porous characterization of activated carbon prepared from pyrolysis of biomass by two-stage procedure at low activation temperature and it's the adsorption of iodine, J. Anal. Appl. Pyrolysis 104 (2013) 378–383, https://doi.org/10.1016/j.jaap.2013.06.009.
[40] A.A. Ceyhan, Ö. Şahîn, C. Saka, A. Yalçın, A novel thermal process for activated carbon production from the vetch biomass with air at low temperature by two-stage procedure, J. Anal. Appl. Pyrolysis 104 (2013) 170–175, https://doi.org/10.1016/j.jaap.2013.08.007.
[41] L. Wu, H. Ma, Z. Yan, Q. Xu, Z. Li, Improving catalyst performance of Ni-CaO-C to enhance H2 production from biomass steam gasification through induction heating technology, Energy Convers. Manag. 270 (2022) 116242, https://doi.org/10.1016/j.enconman.2022.116242.
[42] Y. Zhou, G. Liu, J. Liu, Y. Xiao, T. Wang, Y. Xue, Magnetic biochar prepared by electromagnetic induction pyrolysis of cellulose: biochar characterization, mechanism of magnetization and adsorption removal of chromium (vi) from aqueous solution, Bioresour. Technol. 337 (2021) 125429, https://doi.org/10.1016/j.biortech.2021.125429.
[43] W. Wang, G. Tuci, C. Duong-Viet, Y. Liu, A. Rossin, L. Luconi, J. Nhut, L. Dinh, C. P. Huu, G. Giambastiani, Induction heating: an enabling technology for the heat management in catalytic processes, ACS Catal. 9 (9) (2019) 7921–7935, https://doi.org/10.1021/acscatal.9b02471.
[44] O.S. Sabogal, S. Valin, S. Thiery, S. Salvador, Design and thermal characterization of an induction-heated reactor for pyrolysis of solid waste, Chem. Eng. Res. Des. 173 (2021) 206–214, https://doi.org/10.1016/j.cherd.2021.07.018.
[45] P. Mocho, J. Bourhis, P.L. Cloirec, Heating activated carbon by electromagnetic induction, Carbon 34 (7) (1996) 851–856, https://doi.org/10.1016/0008-6223(96)00053-x.
[46] P. Muley, C. Henkel, K. Abdollahi, D. Boldor, Pyrolysis and catalytic upgrading of pinewood sawdust using an induction heating reactor, Energy Fuels 29 (11) (2015) 7375–7385, https://doi.org/10.1021/acs.energyfuels.5b01878.
[47] A.A. Ceyhan, Ö. Şahîn, O. Baytar, C. Saka, Surface and porous characterization of activated carbon prepared from pyrolysis of biomass by two-stage procedure at low activation temperature and it's the adsorption of iodine, J. Anal. Appl. Pyrolysis 104 (2013) 378–383, https://doi.org/10.1016/j.jaap.2013.06.009.
[48] C.D. Stasi, G. Greco, R.L. Canevesi, M. Izquierdo, V. Fierro, A. Celzard, B. González, J.J. Manyà, Influence of activation conditions on textural properties and performance of activated biochars for pyrolysis vapors upgrading, Fuel 289 (2021) 119759, https://doi.org/10.1016/j.fuel.2020.119759.
[49] N.L. Panwar, A. Pawar, Influence of activation conditions on the physicochemical properties of activated biochar: a review, Biomass.. Conv. Bioref. 12 (2022) 925–947, https://doi.org/10.1007/s13399-020-00870-3.
[50] U.D. Hamza, N.S. Nasri, N.S. Amin, J. Mohammed, H.M. Zain, Characteristics of oil palm shell biochar and activated carbon prepared at different carbonization times, Desalin. Water Treat. 57 (17) (2016) 7999–8006, https://doi.org/10.1080/19443994.2015.1042068.
[51] Ç. Murtazaoğlu, İ. Teğin, C. Saka, Facile hydrogen peroxide modification of activated carbon particles produced by potassium hydroxide activation for removal of heavy metals from aqueous solutions, Diam. Relat. Mater. 136 (2023) 110049, https://doi.org/10.1016/j.diamond.2023.110049.
[52] Ö. Şahîn, C. Saka, Preparation and characterization of activated carbon from acorn shell by physical activation with h2o–co2 in two-step pretreatment, Bioresour. Technol. 136 (2013) 163–168, https://doi.org/10.1016/j.biortech.2013.02.074.
[53] P. Kuo, Z. Sun, F. Özdemir, M. Aziz, W. Wu, Co2 utilization in chemical looping gasification and co-gasification of lignocellulosic biomass components over iron-based oxygen carriers: thermogravimetric behavior, synergistic effect, and reduction characteristics, J. Environ. Chem. Eng. 11 (3) (2023) 109971, https://doi.org/10.1016/j.jece.2023.109971.
[54] J. Niu, Y. Shen, H. Zhang, L. Li, S. Guo, Preparation of highly microporous activated carbon by utilizing inherent iron in coal through CO2 and steam co-activation for improving CO2 capture and methylene blue removal, Fuel 371 (2024) 132069, https://doi.org/10.1016/j.fuel.2024.132069.
[55] A. Bridgwater, Review of fast pyrolysis of biomass and product upgrading, Biomass.. Bioenergy 38 (2012) 68–94, https://doi.org/10.1016/j.biombioe.2011.01.048.
[56] A. Demirbaş, Effects of temperature and particle size on bio-char yield from pyrolysis of agricultural residues, J. Anal. Appl. Pyrolysis 72 (2) (2004) 243–248, https://doi.org/10.1016/j.jaap.2004.07.003.
[57] S.A. Channiwala, P. Parikh, A unified correlation for estimating hhv of solid, liquid and gaseous fuels, Fuel 81 (8) (2002) 1051–1063, https://doi.org/10.1016/s0016-2361(01)00131-4.
[58] Y. Chen, L. Wang, M. Zhao, H. Ma, D. Chen, Y. Zhang, J. Zhou, Comparative study on the pyrolysis behaviors of pine cone and pretreated pine cone by using tga–ftir and pyrolysis-gc/ms, ACS Omega 6 (5) (2021) 3490–3498, https://doi.org/10.1021/acsomega.0c04456.
[59] S.L. Dias, C.L. Neto, V.G. Ferreira, J.C. Vaghetti, G.B. Machado, O. Bianchi, Exploring the thermal degradation of pine nut shells: a study on biochar production and its efficacy in cationic dye adsorption from water, Biomass.. Conv. Bioref. 15 (2024) 5975–5995, https://doi.org/10.1007/s13399-024-05470-z.
[60] X. Xu, R. Chen, R. Pan, D. Zhang, Pyrolysis kinetics, thermodynamics, and volatiles of representative pine wood with thermogravimetry–fourier transform infrared analysis, Energy Fuels 34 (2) (2020) 1859–1869, https://doi.org/10.1021/acs.energyfuels.9b03872.
[61] S. Mandal, J. Haydary, S. Gangil, J. Husár, P.C. Jena, T.K. Bhattacharya, Inferences from thermogravimetric analysis of pine needles and its chars from a pilot-scale screw reactor, Chem. Pap. 74 (2) (2019) 689–698, https://doi.org/10.1007/s11696-019-00998-1.
[62] L. Guo, X. Gao, W. Gao, H. Wu, X. Wang, S. Sun, Y. Wei, Y. Kugue, X. Guo, J. Sun, N. Tsubaki, High-yield production of liquid fuels in co2 hydrogenation on a zeolite-free Fe-based catalyst, Chem. Sci. 14 (1) (2023) 171–178, https://doi.org/10.1039/d2sc05047a.
[63] F. Menegazzo, R. Snyders, C. Bittencourt, M.D. Carmen Bello Pinzon, E. Ghedini, M. Signoretto, From waste to adsorbent: properties of CO2-activated biochars from pistachio hulls and walnut shells for advanced water remediation, Bioresour. Technol. 439 (2025) 133367, https://doi.org/10.1016/j.biortech.2025.133367.
[64] M. Plaza, I. Durán, F. Rubiera, C. Pevida, Co 2 adsorbent pellets produced from pine sawdust: effect of coal tar pitch addition, Appl. Energy 144 (2015) 182–192, https://doi.org/10.1016/j.apenergy.2014.12.090.
[65] L. Zhou, Z. Yang, D. Wei, H. Zhang, W. Lu, Application of Fe based composite catalyst in biomass steam gasification to produce hydrogen rich gas, Front. Chem. 10 (2022), https://doi.org/10.3389/fchem.2022.882787.
[66] R. Roncancio, M.S. Ulcay, J.E. Arango, J.P. Gore, Experimental study of CO2 corn stover char gasification using iron nitrate as a catalyst under a high-pressure environment, Fuel 267 (2020) 117237, https://doi.org/10.1016/j.fuel.2020.117237.
[67] P. Lv, J. Wang, Y. Bai, X. Song, W. Su, G. Yu, Y. Ma, CO2 gasification of petroleum coke with use of iron-based waste catalyst from F-T synthesis, Thermochim. Acta 711 (2022) 179205, https://doi.org/10.1016/j.tca.2022.179205.
[68] J. Luo, G. Gong, C. Cui, S. Sun, J. Lin, R. Ma, J. Sun, Microwave-induced one-pot preparation of bifunctional N-Fe/BC catalysts and oriented production of phenol-enriched bio-oil from biomass pyrolysis: catalyst synthesis, performance evaluation, and mechanism insight via theoretical calculations, ACS Catal. 12 (18) (2022) 11318–11339, https://doi.org/10.1021/acscatal.2c01841.
[69] P. Lahijani, Z. Zainal, A.R. Mohamed, Catalytic effect of iron species on CO2 gasification reactivity of oil palm shell char, Thermochim. Acta 546 (2012) 24–31, https://doi.org/10.1016/j.tca.2012.07.023.
[70] H. Liu, C. Ye, Z. Ye, Z. Zhu, Q. Wang, Y. Tang, G. Luo, W. Guo, C. Dong, G. Li, Y. Xu, Q. Wang, Catalytic cracking and catalyst deactivation/regeneration characteristics of Fe-loaded biochar catalysts for tar model compound, Fuel 334 (2023) 126810, https://doi.org/10.1016/j.fuel.2022.126810.
[71] A. Khajeh, S. Masoumi, L. Wang, A. Shahbazi, Effects of various carbon-supported iron catalysts on tar removal efficiency and syngas yield during catalytic biomass gasification, J. Environ. Chem. Eng. 11 (5) (2023) 110884, https://doi.org/10.1016/j.jece.2023.110884.
[72] L. Wu, Z. Yan, J. Xie, Q. Xu, Z. Li, Enhancing the catalytic h2 production performance of magnetic ni-fe2o3-c catalyst in biomass steam gasification using electromagnetic induction heating, Bioresour. Technol. 402 (2024) 130844, https://doi.org/10.1016/j.biortech.2024.130844.
[73] P. Kim, A.S. Johnson, C.W. Edmunds, M. Radosevich, F. Vogt, T.G. Rials, N. Labbé, Surface functionality and carbon structures in lignocellulosic-derived biochars produced by fast pyrolysis, Energy Fuels 25 (10) (2011) 4693–4703, https://doi.org/10.1021/ef200915s.
[74] D.W. Rutherford, R.L. Wershaw, C.E. Rostad, C.N. Kelly, Effect of formation conditions on biochars: compositional and structural properties of cellulose, lignin, and pine biochars, Biomass.. Bioenergy 46 (2012) 693–701, https://doi.org/10.1016/j.biombioe.2012.06.026.
[75] E.A. Varol, Ü. Mutlu, Tga-ftir analysis of biomass samples based on the thermal decomposition behavior of hemicellulose, cellulose, and lignin, Energies 16 (9) (2023) 3674, https://doi.org/10.3390/en1609367.
[76] B. Li, D. Liu, D. Lin, X. Xie, S. Wang, H. Xu, J. Wang, Y. Huang, S. Zhang, X. Hu, Changes in biochar functional groups and its reactivity after volatile–char interactions during biomass pyrolysis, Energy Fuels 34 (11) (2020) 14291–14299, https://doi.org/10.1021/acs.energyfuels.0c03243.
[77] H. Yang, Z. Dong, B. Liu, Y. Chen, M. Gong, S. Li, H. Chen, A new insight of lignin pyrolysis mechanism based on functional group evolutions of solid char, Fuel 288 (2021) 119719, https://doi.org/10.1016/j.fuel.2020.119719.
[78] S. Zhang, S. Yu, Q. Li, B.A. Mohamed, Y. Zhang, H. Zhou, Insight into the relationship between co2 gasification characteristics and char structure of biomass, Biomass. Bioenergy 163 (2022) 106537, https://doi.org/10.1016/j.biombioe.2022.106537.

[79] X. Zou, M. Zhai, G. Liu, T. Wang, G. Li, Y. Zhang, R. Liaquat, In-depth understanding of the microscopic mechanism of biochar carbonaceous structures during thermochemical conversion: pyrolysis, combustion and gasification, Fuel 361 (2024) 130732, https://doi.org/10.1016/j.fuel.2023.130732.

[80] R. Bardestani, S. Kaliaguine, Steam activation and mild air oxidation of vacuum pyrolysis biochar, Biomass. Bioenergy 108 (2018) 101–112, https://doi.org/10.1016/j.biombioe.2017.10.011.

[81] Z. Xu, M. He, X. Xu, X. Cao, D.C. Tsang, Impacts of different activation processes on the carbon stability of biochar for oxidation resistance, Bioresour. Technol. 338 (2021) 125555, https://doi.org/10.1016/j.biortech.2021.125555.